arXiv:1512.00838v1 [astro-ph.HE] 2 Dec 2015

A large scale dynamo and magnetoturbulence in rapidly rotating core-collapse supernovae

Philipp Mösta[1], Christian D. Ott[1], David Radice[1], Luke F. Roberts[1], Erik Schnetter[2,3,4], & Roland Haas[5]

Originally submitted version of Nature letter doi:10.1038/nature15755

[1]*TAPIR, Walter Burke Institute for Theoretical Physics, Mailcode 350-17, California Institute of Technology, Pasadena, CA 91125, USA, pmoesta@tapir.caltech.edu*

[2]*Perimeter Institute for Theoretical Physics, Waterloo, ON, Canada*

[3]*Department of Physics, University of Guelph, Guelph, ON, Canada*

[4]*Center for Computation & Technology, Louisiana State University, Baton Rouge, LA, USA*

[5]*Max Planck Institute for Gravitational Physics, Am Mühlenberg 1, 14476 Potsdam-Golm, Germany*

Magnetohydrodynamic (MHD) turbulence is of key importance in many high-energy astrophysical systems, including black-hole accretion disks, protoplanetary disks, neutron stars, and stellar interiors. MHD instabilities can amplify local magnetic field strength over very short time scales [1–3], but it is an open question whether this can result in the creation of a large scale ordered and dynamically relevant field. Specifically, the magnetorotational instability (MRI) has been suggested as a mechanism to grow magnetar-strength magnetic field ($\gtrsim 10^{15}$ G) and magnetorotationally power the explosion [4–8] of a rotating massive star [9,10]. Such stars are progenitor candidates for type Ic-bl hypernova explosions that involve rel-

ativistic outflows (e.g. [11,12]) and make up all supernovae connected to long gamma-ray bursts (GRBs) [13,14]. We have carried out global 3D general-relativistic magnetohydrodynamic (GRMHD) turbulence simulations that resolve the fastest growing mode (FGM) of the MRI. We show that MRI-driven MHD turbulence in rapidly rotating protoneutron stars produces a highly efficient inverse cascade of magnetic energy. This builds up magnetic energy on large scales whose magnitude rivals the turbulent kinetic energy. We find a large-scale ordered toroidal field along the rotation axis of the protoneutron star that is consistent with the formation of bipolar magnetorotationally driven outflows. Our results demonstrate that rapidly rotating massive stars are plausible progenitors for both type Ic-bl supernovae [12,15,16] and long GRBs, present a viable formation scenario for magnetars, and may account for potentially magnetar-powered superluminous supernovae [17].

A magnetised fluid is unstable to weak-field shearing modes in the presence of a negative angular velocity gradient that is not compensated for by compositional or entropy gradients of the fluid [3]. For rotating stellar collapse, it was demonstrated that the general conditions for the MRI to activate hold [9] and studying the MRI in this context has been a very active topic of investigation. Doing so numerically, however, is challenging since capturing the FGM of the instability requires high resolution (~ 10 grid zones per MRI FGM wavelength $\lambda_{\rm MRI,FGM} \propto |B|$). For protoneutron stars formed after the collapse of an iron core of a massive star, this requires linear resolutions of $dx \sim 10 - 100\,{\rm m}$ for precollapse magnetic fields of $10^9 - 10^{10}\,{\rm G}$. Current state of the art 3D adaptive mesh-refinement (AMR) simulations reach typical resolution of $dx \sim 750 - 1000\,{\rm m}$ in the shear layer near the protoneutron star (e.g. [8]) and obtain the field strength to power a magne-

torotational explosion ($\gtrsim 10^{15}$ G) by flux-compression ($B \propto \rho^{2/3}$, amplification by a factor $\sim 10^3$) from unrealistically high seed fields ($|B| \geq 10^{12}$ G precollapse). The MRI has been studied with local [18] or semi-global [19] high-resolution shearing box simulations in 3D or with global 2D simulations [20]. The effects of neutrino viscosity and drag on the MRI have also been studied, e.g. [21]. All of these simulations were either not able to capture the inherently 3D saturation behaviour of the MRI since their assumed symmetries or domain sizes prevent secondary parasitic instabilities [22,23] or only studied local effects. Large-scale dynamo action [24,25] has been suggested as a means of building up large scale magnetic field in rapidly rotating protoneutron stars, thereby providing a formation scenario for magnetars [26,27]. Direct numerical simulations of this process have mostly been carried out in the context of simplified scenarios in dynamo theory with an explicit driving of turbulence at specific scales (e.g. [28] and references therein).

Here, we study MHD turbulence in the shear layer around a rapidly rotating protoneutron star using high-resolution (~ 10 times higher than previous simulations) global 3D GRMHD simulations. We take initial conditions from a full 3D GRMHD AMR simulation of stellar collapse in a rapidly spinning progenitor star (initial spin period of the fusion core $P_0 = 2.25\,\mathrm{s}$ before collapse, spin period of the protoneutron star after core bounce $P_{\rm PNS} = 1.18\,\mathrm{ms}$) at $t_{\rm map} = 20\,\mathrm{ms}$ after core bounce. The initial maximum poloidal magnetic field of $10^{10}\,\mathrm{G}$ is amplified during and after collapse to a maximum $\simeq 7 \cdot 10^{14}\,\mathrm{G}$ at the time of mapping and linear winding [29] builds up maximum toroidal field of $\simeq 7 \cdot 10^{14}\,\mathrm{G}$ close to the rotation axis of the protoneutron star and $\simeq 3 \cdot 10^{14}\,\mathrm{G}$ in the equatorial region. We carry out simulations in four resolutions, $dx = \{500\,\mathrm{m}, 200\,\mathrm{m}, 100\,\mathrm{m}, 50\,\mathrm{m}\}$, adopt a domain size of $66.5\,\mathrm{km}$ in x and y direction and

$133\,\mathrm{km}$ in z direction (rotation axis), and employ a 90° rotational symmetry in the xy-plane (no symmetry in z). This allows us to study the MRI-unstable layer surrounding the core of the proto-neutron star with unprecedented resolution with fully self-consistent global 3D simulations of MHD turbulence in stellar collapse.

The two lowest resolution simulations show no or only minor toroidal magnetic field amplification consistent with not resolving the FGM of the MRI. The toroidal field in the two highest resolution simulations exhibits exponential growth soon after the start of our simulations (Fig. 1). The poloidal magnetic field evolution follows the toroidal one closely (Extended Data Fig. 2). The initial transition to exponential growth in both the global maximum toroidal field (left panel Fig. 1) and the maximum toroidal field in a box with height $7.5\,\mathrm{km}$ above and below the equatorial plane (right panel Fig. 1) is nearly identical and indicates that we resolve the FGM of the MRI with the $100\,\mathrm{m}$ simulation. This is consistent with our background flow stability analysis of the AMR simulation before mapping (see Extended Data Fig. 1). The observed growth rate of $\tau \simeq 0.5\,\mathrm{ms}$ agrees well with the analytically predicted growth rate of the FGM from linear analysis. The field evolution quickly becomes non-linear and this rapid growth reaches a fully turbulent saturated state within $3\,\mathrm{ms}$. The turbulent saturated toroidal field strength agrees to within a factor of two between the two highest resolution simulations ($100\,\mathrm{m}$ and $50\,\mathrm{m}$). Once non-linear field strength is reached, secondary modes and couplings between individual modes become important. The final turbulent saturation field differs slightly between resolutions because finite resolution in this regime prevents unstable MRI modes just away from the FGM from growing at the maximum rate. However, since modes with wavelengths much smaller than $\lambda_{\mathrm{MRI,FGM}}$ are stable, these differences decrease with

increasing resolution and we expect our results to hold when even higher-resolution simulations become computationally accessible. This is supported by the fact that the local features of our global 3D simulations are consistent with previous higher resolution ($dx \simeq 10\,\mathrm{m}$) local simulations [18]. The resolution dependence of the magnetic field in the turbulent state is striking (Fig. 2). While the $500\,\mathrm{m}$ and $200\,\mathrm{m}$ simulations show none to only mild turbulence, the $100\,\mathrm{m}$ and $50\,\mathrm{m}$ simulations develop a fully turbulent shear layer around the protoneutron star. We observe radial filaments of magnetic field that oscillate from negative to positive values on a length scale of $1\,\mathrm{km}$, consistent with the predicted wavelength of the FGM of the MRI (see Extended Data Fig. 1). These structures resemble channel flow formation observed in shearing box simulations [18] but do not stay coherent due to the background flow. Similar, non-coherent filaments were also observed in the 2D global simulations of [20].

The turbulent kinetic and electromagnetic energy spectra calculated from our simulations are shown in Fig. 3. Initially, the turbulent kinetic energy, which is nearly constant in time, is several orders of magnitude larger across all scales than the electromagnetic energy. The spectrum is fitted well with a $k^{-5/3}$ scaling dependence as expected in Kolmogorov theory. The lack of an exponential turnoff at large k in the turbulent kinetic energy is due to the inclusion of the nearly discontinuous density falloff at the edge of the protoneutron star core (at $r \simeq 12\,\mathrm{km}$) in the calculation of the spectrum. In contrast, the electromagnetic energy is highly time and resolution dependent. While the low resolution shows little evolution away from the initial spectrum, the higher resolution calculations saturate at larger and larger energy at large k (top left panel Fig. 3). The saturation value at large and intermediate k is within a factor of 3 of equipartition with the tur-

bulent kinetic energy in the $50\,\mathrm{m}$ calculation. Within the first $3\,\mathrm{ms}$ there is a rapid transition into a fully turbulent state at large k (top right panel, Fig. 3). This correlates well with the observed saturation at $t-t_{\mathrm{map}} \simeq 3\,\mathrm{ms}$ of the maximum toroidal field shown in Fig. 1. After saturation is reached at large k, we observe an inverse cascade of energy causing growth of large scale electromagnetic energy peaked at $k = 4$, which corresponds to a length scale of $5\,\mathrm{km}$ for our domain. This is well below the driving scale of the FGM of the MRI ($k \simeq 20$) and consistent with the structures evident in the right lower panel of Fig. 2 and the rightmost panel of Fig. 4. The growth in the first $7\,\mathrm{ms}$ is fitted well by an exponential with e-folding time $\tau = 3.5\,\mathrm{ms}$ superposed with a $2\,\mathrm{ms}$ modulation that corresponds roughly to the Alfvén crossing time across the shear layer ($t_{\mathrm{A,shear}} \sim 2\,\mathrm{ms}$). We observe a transition away from clean exponential growth for $t-t_{\mathrm{map}} \geq 7\,\mathrm{ms}$, which may be caused by the magnetic field becoming dynamically relevant. Here, the growth at $k = 4$ is better described by a linear fit. In an inverse cascade the energy is expected to reach approximately the same relative saturation value (with respect to the driving turbulent kinetic energy) at all k's with sufficiently long evolution time [24,25]. We find evidence for this in the range $10 \leq k \leq 50$ where the magnetic energy spectrum begins to evolve towards a similar power-law scaling as the turbulent kinetic energy. Assuming this holds also at smaller k, we extrapolate the growth of magnetic energy based on the linear fit (bottom panel, Fig. 3). We expect to reach saturation electromagnetic energy at small k within $t - t_{\mathrm{map}} \simeq 60\,\mathrm{ms}$. The observed difference between the $100\,\mathrm{m}$ and $50\,\mathrm{m}$ resolution calculations in the saturation energy at large k and in the inverse energy cascade indicates that the turbulent state is not fully captured with the $100\,\mathrm{m}$ simulation and that the efficiency of the inverse cascade may still increase when going to even higher resolution than $50\,\mathrm{m}$.

Our results indicate that the electromagnetic energy will rival the turbulent kinetic energy and dominate the less efficient neutrino heating independent of when a gain layer is established ($t - t_{\rm map} \sim 50 - 100\,{\rm ms}$) [7,30]. Therefore MHD stresses are likely the dominant factor in reviving the stalled shock in rapidly rotating progenitors. Furthermore, we observe formation of large-scale structured toroidal magnetic field near the rotation axis of the protoneutron star in the later stages of the $50\,{\rm m}$ simulation (right panel, Fig. 4). This large scale field is not present in the initial data (left panel, Fig. 4), nor does it develop in the lower resolution cases (centre panel, Fig. 4). This magnetar-strength toroidal field close to the rotation axis is a strong indication that hoop stresses which favour the formation of MHD-powered outflows are present along the poles [5,6,29]. Our findings have significant implications for stellar collapse in rapidly rotating massive stars. The MRI is a weak-field instability (i.e. its growth rate $\tau_{\rm MRI}$ does not depend on the strength of the magnetic field) and the observed rapid e-folding time of $\tau \simeq 0.5\,{\rm ms}$ is short enough such that the scenario presented here is viable even for much weaker initial seed fields. In addition, the MRI was shown to operate efficiently in purely toroidal, mixed poloidal/toroidal and random magnetic field configurations [3]. Hence, we expect our results to hold for arbitrary precollapse magnetic field configurations. This makes MHD-driven explosions a likely scenario in rapidly rotating progenitors independent of the initial magnetisation of the star. Additionally, the large-scale build up of magnetic field in the shear layer of the protoneutron star demonstrates that MRI-driven turbulence poses a promising mechanism to form pulsars and magnetars in rapidly rotating stellar collapse. This indicates that rapidly rotating massive stars can also account for potentially magnetar-powered superluminous supernovae [17].

Online Content Methods, along with any additional Extended Data display items and Source Data, are available in the online version of the paper; references unique to these sections appear only in the online paper.

Acknowledgements The authors would like to thank S. Couch, J. Zrake, D. Tsang, C. Wheeler, E. Bentivegna and I. Hinder for discussions. This research was partially supported by NSF grants AST-1212170, PHY-1151197, OCI-0905046, and the Sherman Fairchild Foundation. The simulations were carried out on NSF/NCSA BlueWaters (PRAC ACI-1440083).

Contributions **P.M.**: Project planning, simulations, simulation analysis, visualisation, interpretation, manuscript preparation. **C.D.O.**: Group and project leadership, idea for the project, project planning, interpretation, manuscript preparation. **D.R.**: Simulation analysis, interpretation, simulation code development, manuscript preparation. **L.F.R.**: Interpretation, manuscript review. **E.S.**: Simulation code development, manuscript review. **R.H.**: Simulation code development, visualisation software development, manuscript review.

Author Information All computer code used in this study that is not already open source, will be made available under http://stellarcollapse.org. Reprints and permissions information is available at www.nature.com/reprints. The authors declare that they have no competing financial interests. Correspondence and requests for materials should be addressed to Philipp Mösta. (email: pmoesta@tapir.caltech.edu).

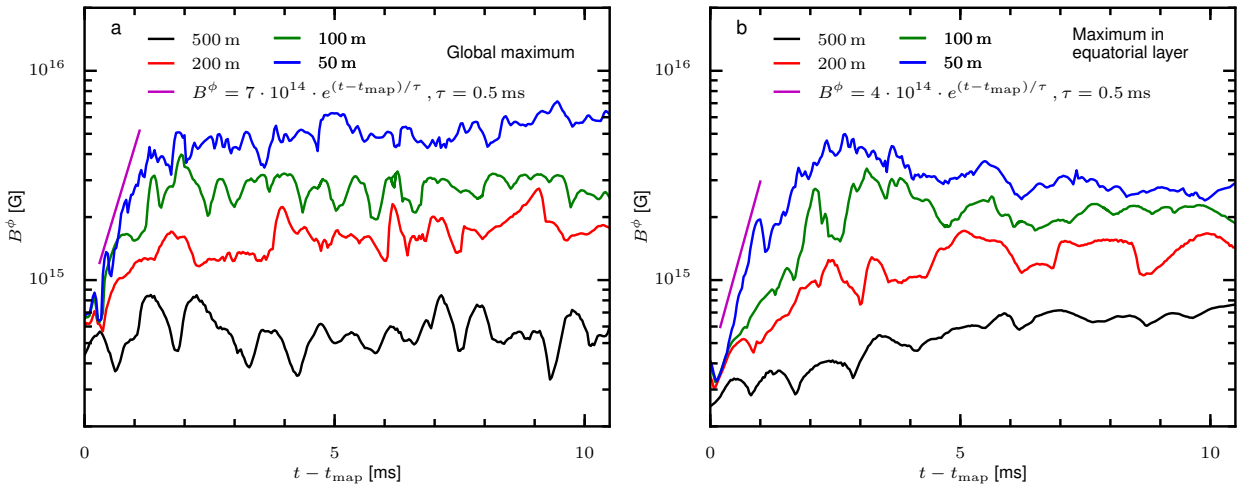

Figure 1: Evolution of the maximum toroidal magnetic field. Both panels show the maximum toroidal magnetic field as a function of time for the four resolutions $500\,\mathrm{m}$, $200\,\mathrm{m}$, $100\,\mathrm{m}$, and $50\,\mathrm{m}$. The left panel shows the global maximum field, the right panel the maximum field in a thin layer above and below the equatorial plane ($-7.5\,\mathrm{km} \leq z \leq 7.5\,\mathrm{km}$). The magenta line indicates exponential growth with an e-folding time $\tau = 0.5\,\mathrm{ms}$

.

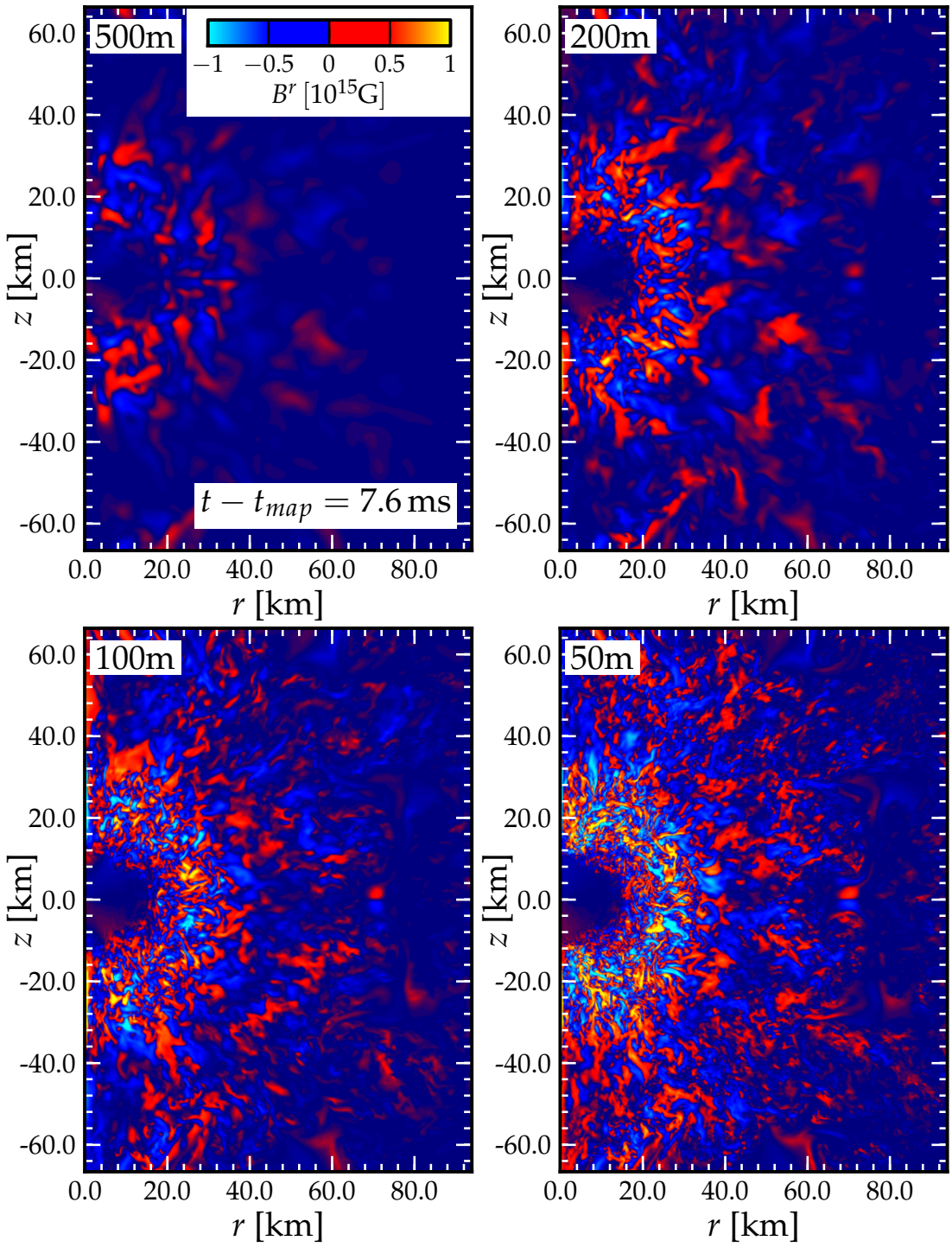

Figure 2: Visualisation of the radial component of the magnetic field in 2D slices. 2D rz-slices at azimuth $\phi = 45°$ for the four resolutions $500\,\mathrm{m}$, $200\,\mathrm{m}$, $100\,\mathrm{m}$, and $50\,\mathrm{m}$ at $t - t_{\mathrm{map}} = 7.6\,\mathrm{ms}$. The colourmap ranges from positive 10^{15} G (yellow) to negative 10^{15} G (light blue).

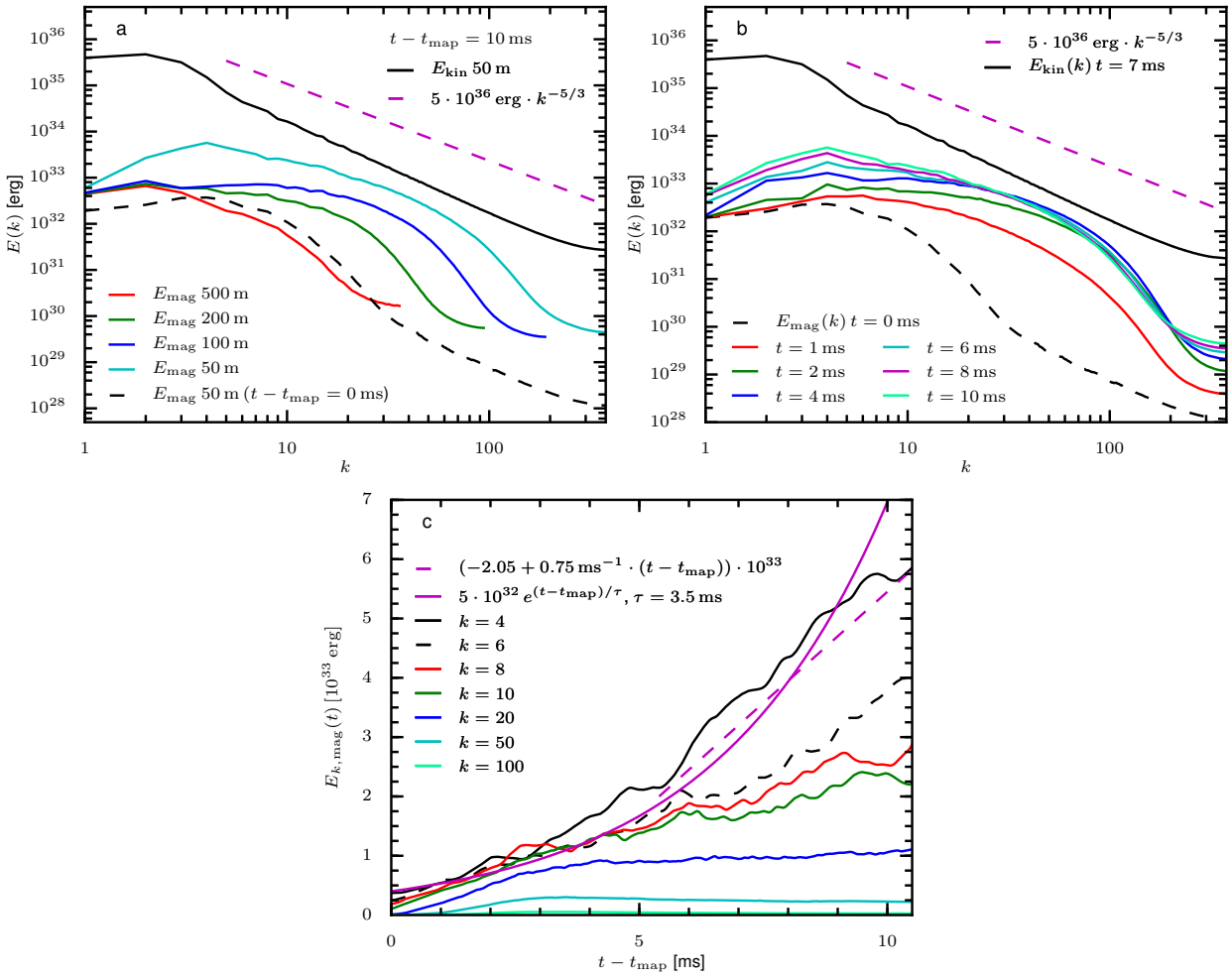

Figure 3: Turbulent kinetic and electromagnetic energy spectra. The top two panels show the energy as a function of dimensionless wavenumber k. The top left panel compares the electromagnetic energy across all four resolutions. The top right panel shows a time series of electromagnetic energy spectra for the $50\,\mathrm{m}$ simulation only. In the two upper panels the turbulent kinetic energy as computed from the $50\,\mathrm{m}$ simulation, a line indicating Kolmogorov scaling ($k^{-5/3}$), and the initial electromagnetic energy spectrum are shown. The bottom panel shows the electromagnetic energy at a given wavenumber E_k versus time and an exponential and linear fit.

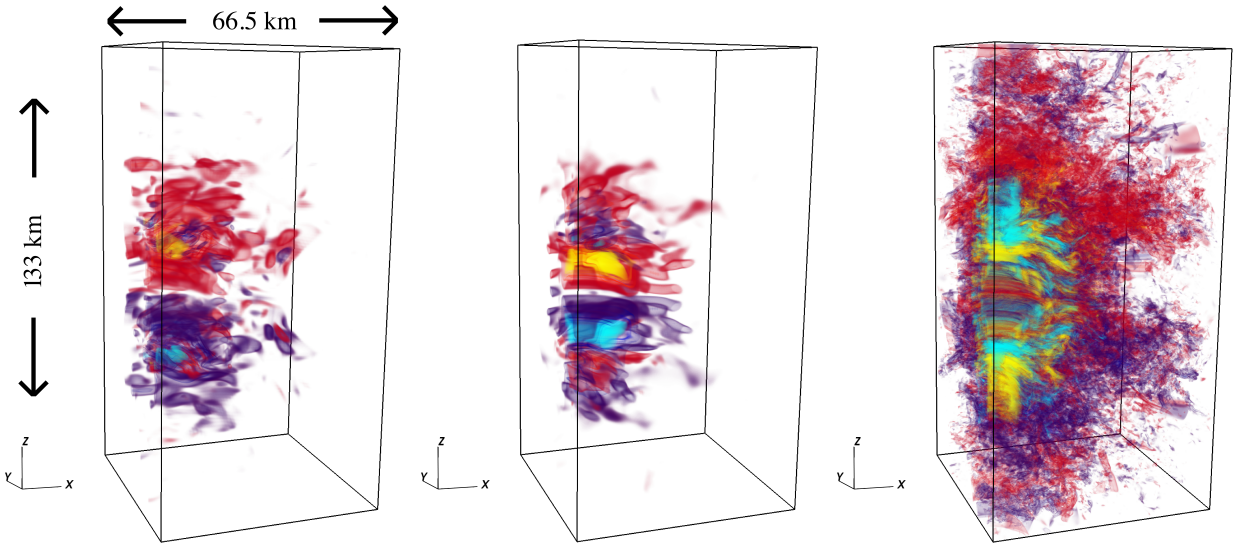

Figure 4: 3D volume renderings of the toroidal magnetic field. All panels show ray-casting volume renderings of B^{ϕ}. The rotation axis z is the vertical and the volume renderings are generated with a varying-alpha colourmap. Yellow indicates positive field of strength $10^{15}\,\mathrm{G}$ and red indicates weaker positive field. Light blue corresponds to negative field of $10^{15}\,\mathrm{G}$, while blue indicates weaker negative field. The left most panel shows the initial conditions for our simulations, the middle panel the $500\,\mathrm{m}$ simulation at time $t - t_{\mathrm{map}} = 10\,\mathrm{ms}$ and the right panel the $50\,\mathrm{m}$ simulation at $t - t_{\mathrm{map}} = 10\,\mathrm{ms}$.

Methods

Initial conditions: Stellar collapse simulation

We start by performing a dynamical spacetime GR ideal MHD simulation with AMR of the 25-$M_\odot$ (at zero-age-main-sequence) presupernova model E25 from [31] with initial conditions for differential rotation as in [8] (initial central angular velocity of the fusion core $2.8\,\mathrm{rad\,s^{-1}}$, $x_0 = 500\,\mathrm{km}$ and $z_0 = 2000\,\mathrm{km}$). This model could be considered as a type Ic-bl/hypernova and long gamma-ray burst progenitor [16]. At the onset of collapse, we set up a modified dipolar magnetic field structure from a vector potential of the form $A_r = A_\theta = 0; A_\phi = B_0(r_0^3)(r^3 + r_0^3)^{-1}\, r \sin\theta$, with $r_0 = 1000\,\mathrm{km}$ as in [8], but with $B_0 = 10^{10}\,\mathrm{G}$. This progenitor seed field is not unreasonable for GRB supernova progenitor cores [16,32]. With the grid setup (9 levels of box-in-box AMR, finest resolution $dx = 375\,\mathrm{m}$) and methods identical to [8,33], we follow this simulation until $20\,\mathrm{ms}$ after core bounce. At this time, the initial supernova shockwave has stalled at a radius of $\simeq 130\,\mathrm{km}$. Both the protoneutron star and the post-shock region have reached a quasi-equilibrium state and the underlying space-time changes only very slowly and secularly, which allows us to carry out subsequent high-resolution GRMHD simulations assuming a fixed background spacetime for $\sim 10 - 20\,\mathrm{ms}$.

Background flow stability analysis

At the time of mapping, the plasma in the shocked region around the protoneutron star is locally unstable to weak-field shearing modes where $\mathcal{C}_{\rm MRI} \equiv (\omega_{BV}^2 + r\frac{d\Omega^2}{dr})/\Omega^2 < 0$ [3,18,34]. Here $\omega_{\rm BV}$ is the Brunt-Väisälä frequency indicating convective stability/instability, $r\frac{d\Omega^2}{dr}$ characterises

the rotational shear, and Ω is the angular velocity. We follow [9,34] and calculate the stability criterion $\mathcal{C}_{\rm MRI}$, and the wavelength $\lambda_{\rm FGM}$ and growth rate $\tau_{\rm FGM}$ of the FGM of the MRI in 2D xy- and xz-slices through our 3D domain. To approximate the background flow in our 3D AMR stellar collapse simulation (which uses refinement in time and therefore has different timesteps on different refinement levels), before mapping, we average in space and time. We first carry out a spatial averaging step with a 3-point stencil in every direction and calculate averaged versions of the state variables of our simulation at every timestep, e.g. the spatially averaged density $\bar{\rho}_i$. Next we calculate a moving time average of the form $\rho_{{\rm av},i} = \alpha \cdot \bar{\rho}_i + (1.0 - \alpha) \cdot \rho_{{\rm av},i-1}$, where i denotes the current timestep and $i-1$ the previous one. We choose a weight function for each dataset in the moving average as $\alpha = 2 \cdot (\Delta t / \Delta t_{\rm coarse} \cdot n + 1.0)^{-1}$, where Δt is the timestep on the current refinement level and $\Delta t_{\rm coarse}$ the timestep of the coarsest level. This choice of weight function guarantees that 86% of the data in the average is comprised of the last n timestep datasets. The timestep size in our AMR simulation on the refinement level containing the shear layer around the protoneutron star is $\Delta t = 5 \times 10^{-4}\,{\rm ms}$ and we choose n such that $\alpha = 2000$, ensuring temporal averaging over a timescale of $\simeq 1\,{\rm ms}$. We calculate $\mathcal{C}_{\rm MRI}$, $\lambda_{\rm FGM}$, and $\tau_{\rm FGM}$ from the space and time averages of the state variables in our simulation (Extended Data Fig. 1).

Mapping to high-resolution computational domain

Next, we map the configuration to a 3D domain with uniform spacing of the form $x, y, z = [-66.5\,{\rm km}, 66.5\,{\rm km}]$ for four resolutions $h = \{500\,{\rm m}, 200\,{\rm m}, 100\,{\rm m}, 50\,{\rm m}\}$. To guarantee divergence-free initial data for the magnetic field, we carry out a constraint projection step after we have inter-

polated the magnetic field to the new domain. This is technically challenging as we have to make sure that all operators used in the projection are consistent in their definition with the discrete form of the divergence operator maintained in our specific implementation of constrained transport [33]. We use a discrete analog of the Helmholtz decomposition [35] to decompose the magnetic field into a discrete curl curl_h and a discrete gradient grad_h,

$$\mathbf{B} = \mathrm{curl}_h\, \mathbf{A} + \mathrm{grad}_h\, \Phi\,, \tag{1}$$

where Φ is a discrete scalar field. The discrete divergence div_h of (1) leads to a discrete Poisson equation

$$\mathrm{div}_h \mathbf{B} = \triangle_h \Phi\,, \tag{2}$$

where $\triangle_h$ is the discrete Laplace operator. We solve (2) augmented with homogeneous Dirichlet boundary conditions to machine precision for Φ using the conjugate gradient solver provided by the PETSc [36] library in combination with the parallel algebraic multi-grid preconditioner HYPRE [37]. We then obtain a divergence free field $\mathbf{B}'$ from the projection

$$\mathbf{B}' = \mathbf{B} - \mathrm{grad}_h \Phi\,. \tag{3}$$

Finally, we recompute $\mathrm{div}_h \mathbf{B}'$ to check that it is zero to floating point precision.

High-resolution turbulence simulations

We perform ideal, fixed background spacetime, GRMHD simulations using the open-source `Einstein Toolkit` [33,38] with WENO5 reconstruction [39,40], the HLLE Riemann solver [41] and constrained transport [42] for maintaining $\mathrm{div}\mathbf{B} = 0$. We employ the $K_0 = 220\,\mathrm{MeV}$ variant of

the finite-temperature nuclear equation of state of [43] and the neutrino leakage/heating approximations described in [44] and [45] with a heating scale factor $f_{\rm heat} = 1.0$. We perform simulations on a domain with uniform spacing of the form $x, y = [0\,{\rm km}, 66.5\,{\rm km}]$ and $z = [-66.5\,{\rm km}, 66.5\,{\rm km}]$ for four resolutions $h = \{500\,{\rm m}, 200\,{\rm m}, 100\,{\rm m}, 50\,{\rm m}\}$ in quadrant symmetry 3D (90-degree rotational symmetry in the xy-plane). We keep all variables at the boundary fixed in time, which is justified by the fact that the boundary flow changes on timescales longer than those simulated. To prevent spurious oscillations in the magnetic field at the outer boundary without affecting the solution in the shear layer around the protoneutron star, we apply diffusivity at the level of the induction equation for the magnetic field via a modified Ohm's law. We choose $\mathbf{E} = -\mathbf{v} \times \mathbf{B} + \eta \mathbf{J}$, where $\mathbf{J} = \nabla \times \mathbf{B}$ is the 3-current density and set $\eta = \eta_0 \cdot (0.5 + 0.5 \tanh{((r - r_{\rm diff})\ b^{-1})})$ with $\eta_0 = 10^{-2}$, $r_{\rm diff} = 40\,{\rm km}$ and $b = 3\,{\rm km}$. That is, we apply diffusivity only in a region outside of radius $r_{\rm diff}$ and transition smoothly over a blending zone with width b to no diffusivity inside $r_{\rm diff}$.

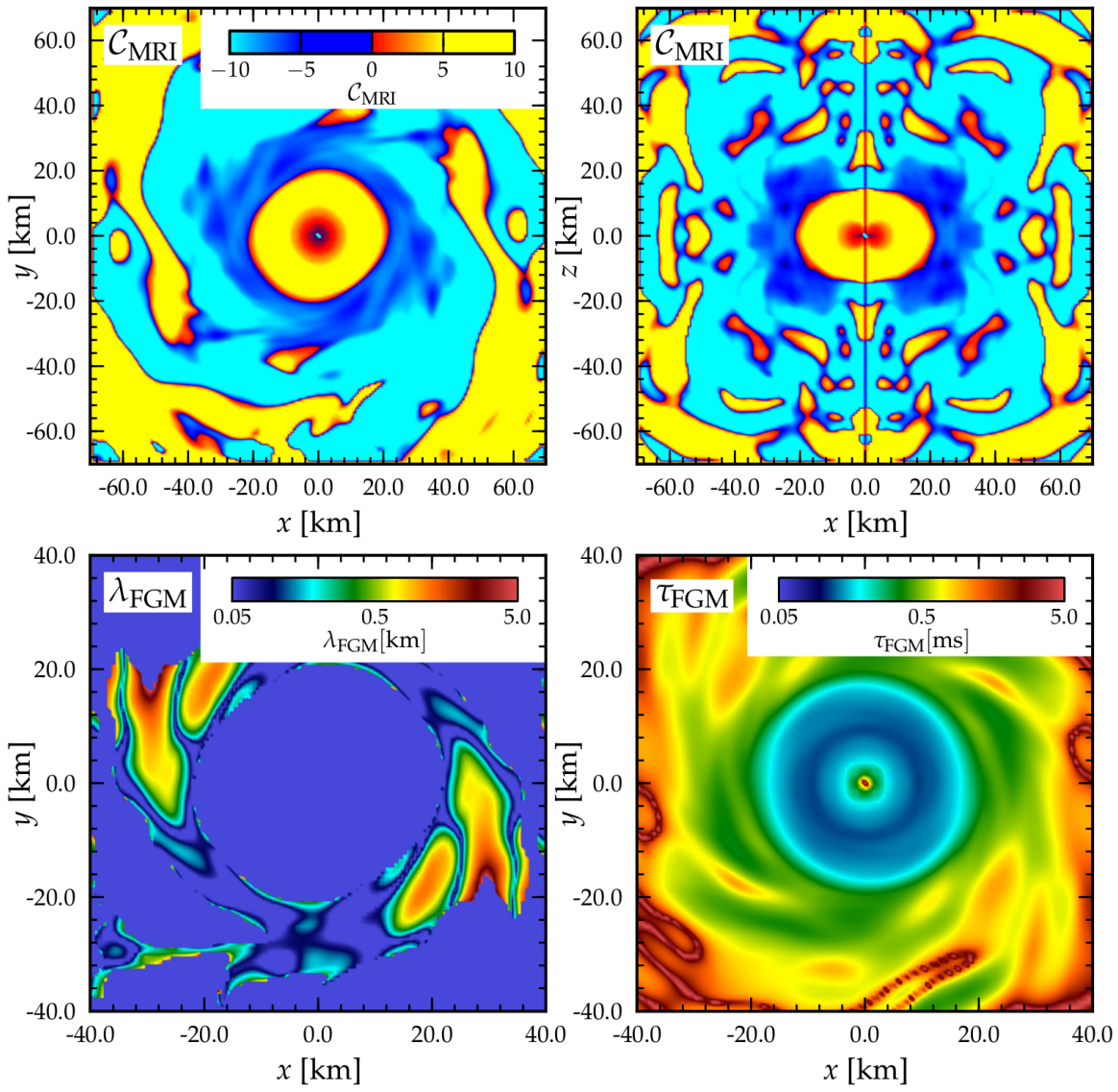

Extended Data Figure 1: Background flow stability analysis. The top two panels show the stability criterion $\mathcal{C}_{\rm MRI}$ 20 ms after core bounce for the initial stellar collapse simulation. The top left panel shows a 2D xy-slice through the 3D domain, the top right panel a xz-slice. Yellow and red indicate regions, which are stable to shearing modes, while dark and light blue colours indicate unstable regions. The bottom left panel shows the wavelength of the FGM of the MRI $\lambda_{\rm FGM}$, the bottom right panel the growth rate of the FGM $\tau_{\rm FGM}$. Both lower panels are zoomed in on the shear layer around the protoneutron star.

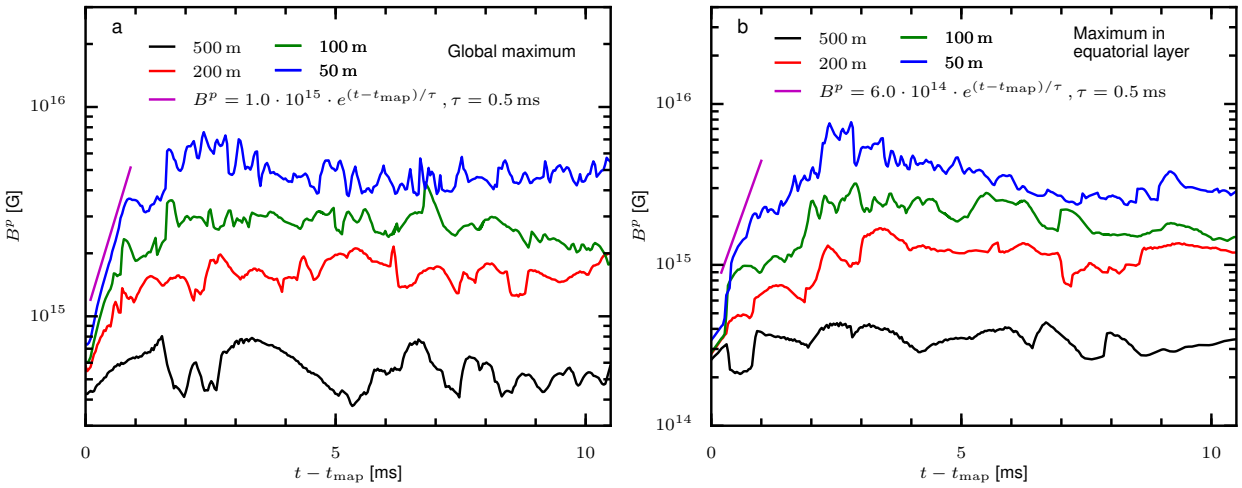

Extended Data Figure 2: Evolution of the maximum poloidal magnetic field. Both panels show the maximum poloidal magnetic field as a function of time for the four resolutions $500\,\mathrm{m}$, $200\,\mathrm{m}$, $100\,\mathrm{m}$, and $50\,\mathrm{m}$. The left panel shows the global maximum field, the right panel the maximum field in a thin layer above and below the equatorial plane ($-7.5\,\mathrm{km} \leq z \leq 7.5\,\mathrm{km}$). The magenta line indicates exponential growth with an e-folding time $\tau = 0.5\,\mathrm{ms}$.

References

1. Chandrasekhar, S. The Stability of Non-Dissipative Couette Flow in Hydromagnetics. *Proceedings of the National Academy of Science* **46**, 253–257 (1960).

2. Fricke, K. Stability of Rotating Stars II. The Influence of Toroidal and Poloidal Magnetic Fields. *Astron. & Astrophys.* **1**, 388 (1969).

3. Balbus, S. A. & Hawley, J. F. A powerful local shear instability in weakly magnetized disks. I—Linear analysis. II—Nonlinear evolution. *Astrophys. J.* **376**, 214 (1991).

4. Bisnovatyi-Kogan, G. S. The Explosion of a Rotating Star As a Supernova Mechanism. *Astron. Zh.* **47**, 813 (1970).

5. LeBlanc, J. M. & Wilson, J. R. A Numerical Example of the Collapse of a Rotating Magnetized Star. *Astrophys. J.* **161**, 541 (1970).

6. Meier, D. L., Epstein, R. I., Arnett, W. D. & Schramm, D. N. Magnetohydrodynamic phenomena in collapsing stellar cores. *Astrophys. J.* **204**, 869 (1976).

7. Burrows, A., Dessart, L., Livne, E., Ott, C. D. & Murphy, J. Simulations of Magnetically Driven Supernova and Hypernova Explosions in the Context of Rapid Rotation. *Astrophys. J.* **664**, 416 (2007).

8. Mösta, P. *et al.* Magnetorotational Core-Collapse Supernovae in Three Dimensions. *Astrophys. J. Letters* **785**, L29 (2014).

9. Akiyama, S., Wheeler, J. C., Meier, D. L. & Lichtenstadt, I. The Magnetorotational Instability in Core-Collapse Supernova Explosions. *Astrophys. J.* **584**, 954 (2003).

10. Thompson, T. A., Quataert, E. & Burrows, A. Viscosity and Rotation in Core-Collapse Supernovae. *Astrophys. J.* **620**, 861 (2005).

11. Soderberg, A. M. *et al.* Relativistic ejecta from X-ray flash XRF 060218 and the rate of cosmic explosions. *Nature* **442**, 1014 (2006).

12. Drout, M. R. *et al.* The First Systematic Study of Type Ibc Supernova Multi-band Light Curves. *Astrophys. J.* **741**, 97 (2011).

13. Modjaz, M. Stellar forensics with the supernova-GRB connection. *Astron. Nachr.* **332**, 434 (2011).

14. Hjorth, J. & Bloom, J. S. The Gamma-Ray Burst - Supernova Connection. In Kouveliotou, C., Wijers, R. A. M. J. & Woosley, S. E. (eds.) *Gamma-Ray Bursts; arXiv:1104.2274* (Cambridge University Press, Cambridge, UK, 2011).

15. Galama, T. J. *et al.* An unusual supernova in the error box of the γ-ray burst of 25 April 1998. *Nature* **395**, 670–672 (1998).

16. Woosley, S. E. & Heger, A. The Progenitor Stars of Gamma-Ray Bursts. *Astrophys. J.* **637**, 914 (2006).

17. Nicholl, M. *et al.* Slowly fading super-luminous supernovae that are not pair-instability explosions. *Nature* **502**, 346–349 (2013).

18. Obergaulinger, M., Cerdá-Durán, P., Müller, E. & Aloy, M. A. Semi-global simulations of the magneto-rotational instability in core collapse supernovae. *Astron. & Astrophys.* **498**, 241 (2009).

19. Masada, Y., Takiwaki, T. & Kotake, K. Magnetohydrodynamic Turbulence Powered by Magnetorotational Instability in Nascent Protoneutron Stars. *Astrophys. J. Letters* **798**, L22 (2015).

20. Sawai, H., Yamada, S. & Suzuki, H. Global Simulations of Magnetorotational Instability in the Collapsed Core of a Massive Star. *Astrophys. J. Letters* **770**, L19 (2013).

21. Guilet, J., Müller, E. & Janka, H.-T. Neutrino viscosity and drag: impact on the magnetorotational instability in protoneutron stars. *Mon. Not. of the Royal Astro. Soc.* **447**, 3992–4003 (2015).

22. Goodman, J. & Xu, G. Parasitic instabilities in magnetized, differentially rotating disks. *Astrophys. J.* **432**, 213 (1994).

23. Pessah, M. E. & Goodman, J. On the Saturation of the Magnetorotational Instability Via Parasitic Modes. *Astrophys. J. Letters* **698**, L72–L76 (2009).

24. Frisch, U., Pouquet, A., Leorat, J. & Mazure, A. Possibility of an inverse cascade of magnetic helicity in magnetohydrodynamic turbulence. *Journal of Fluid Mechanics* **68**, 769–778 (1975).

25. Malkus, W. V. R. Magnetic field generation in electrically conducting fluids. by h. k. moffatt. cambridge university press, 1978. 343 pp. 15.50. *Journal of Fluid Mechanics* **92**, 397–399 (1979).

26. Duncan, R. C. & Thompson, C. Formation of very strongly magnetized neutron stars - Implications for gamma-ray bursts. *Astrophys. J. Letters* **392**, L9–L13 (1992).

27. Thompson, C. & Duncan, R. C. Neutron star dynamos and the origins of pulsar magnetism. *Astrophys. J.* **408**, 194 (1993).

28. Brandenburg, A. & Subramanian, K. Astrophysical magnetic fields and nonlinear dynamo theory. *Phys. Rep.* **417**, 1–209 (2005).

29. Wheeler, J. C., Meier, D. L. & Wilson, J. R. Asymmetric Supernovae from Magnetocentrifugal Jets. *Astrophys. J.* **568**, 807 (2002).

30. Ott, C. D., Burrows, A., Thompson, T. A., Livne, E. & Walder, R. The Spin Periods and Rotational Profiles of Neutron Stars at Birth. *Astrophys. J. Suppl.* **164**, 130 (2006).

31. Heger, A., Langer, N. & Woosley, S. E. Presupernova Evolution of Rotating Massive Stars. I. Numerical Method and Evolution of the Internal Stellar Structure. *Astrophys. J.* **528**, 368 (2000).

32. Wheeler, J. C., Kagan, D. & Chatzopoulos, E. The Role of the Magnetorotational Instability in Massive Stars. *Astrophys. J.* **799**, 85 (2015).

33. Mösta, P. *et al.* GRHydro: a new open-source general-relativistic magnetohydrodynamics code for the Einstein toolkit. *Class. Quantum Grav.* **31**, 015005 (2014).

34. Balbus, S. A. & Hawley, J. F. Instability, turbulence, and enhanced transport in accretion disks. *Reviews of Modern Physics* **70**, 1–53 (1998).

35. Desbrun, M., Kanso, E. & Tong, Y. Discrete differential forms for computational modeling. In *ACM SIGGRAPH 2006 Courses*, SIGGRAPH '06, 39–54 (ACM, New York, NY, USA, 2006).

36. Balay, S. *et al.* PETSc Web page (2015). URL `http://www.mcs.anl.gov/petsc`.

37. Falgout, R. D. & Yang, U. M. hypre: a library of high performance preconditioners. In *Preconditioners, Lecture Notes in Computer Science*, 632–641 (2002).

38. Löffler, F. *et al.* The Einstein Toolkit: a community computational infrastructure for relativistic astrophysics. *Class. Quantum Grav.* **29**, 115001 (2012).

39. Reisswig, C. *et al.* Three-Dimensional General-Relativistic Hydrodynamic Simulations of Binary Neutron Star Coalescence and Stellar Collapse with Multipatch Grids. *Phys. Rev. D.* **87**, 064023 (2013).

40. Tchekhovskoy, A., McKinney, J. C. & Narayan, R. WHAM: A WENO-based general relativistic numerical scheme I: Hydrodynamics. *Mon. Not. of the Royal Astro. Soc.* **379**, 469 (2007).

41. Einfeldt, B. On Godunov type methods for the Euler equations with a general equation of state. In *Shock tubes and waves; Proceedings of the Sixteenth International Symposium, Aachen, Germany, July 26–31, 1987. VCH Verlag, Weinheim, Germany*, 671 (1988).

42. Tóth, G. The $\nabla \cdot B = 0$ Constraint in Shock-Capturing Magnetohydrodynamics Codes. *J. Comp. Phys.* **161**, 605 (2000).

43. Lattimer, J. M. & Swesty, F. D. A Generalized Equation of State for Hot, Dense Matter. *Nucl. Phys. A* **535**, 331 (1991).

44. O'Connor, E. & Ott, C. D. A New Open-Source Code for Spherically-Symmetric Stellar Collapse to Neutron Stars and Black Holes. *Class. Quantum Grav.* **27**, 114103 (2010).

45. Ott, C. D. *et al.* Correlated gravitational wave and neutrino signals from general-relativistic rapidly rotating iron core collapse. *Phys. Rev. D* **86**, 024026 (2012).